ADVANCED FUNCTIONAL MATERIALS
www.afm-journal.de

Whirling-Folded Triboelectric Nanogenerator with High Average Power for Water Wave Energy Harvesting

*Jie An, Zi Ming Wang, Tao Jiang, Xi Liang, and Zhong Lin Wang**

Ocean wave energy, as one of the most abundant resources on the earth, is a promising energy source for large-scale applications. Triboelectric nanogenerators (TENGs) provide a new strategy for water wave energy harvesting; however, its average performance in realistic water wave conditions is still not high. In this work, a whirling-folded TENG (WF-TENG) with maximized space utilization and minimized electrostatic shielding is constructed by 3D printing and printed circuit board technologies. The flexible vortex structure responds easily to multiform wave excitation with improved oscillation frequency. A standard water wave tank is established to generate controllable water waves to characterize the device performance. It is found to be determined by wave conditions and internal structure, which is also revealed by a theoretical dynamical analysis. The WF-TENG can produce a maximum peak power of 6.5 mW and average power of 0.28 mW, which can power a digital thermometer to operate constantly and realize self-powered monitoring on the TENG network to prevent possible damage in severe environments. Moreover, a self-charge-supplement WF-TENG network is proposed to improve the output performance and stability. This study provides an effective strategy for improving the average power and characterizing the performance of spherical TENG towards large-scale blue energy.

1. Introduction

Thousands of inhabited islands, drilling platforms, and marine equipment around the world have been facing great demands for energy, which is now mainly relying on fossil fuels and long-and-weak power grid from the remote land. To alleviate this long-term energy shortage dilemma, developing renewable and sustainable energy sources is highly desirable for in-place power supply.[1] Water wave energy is deemed to be a promising energy source with the advantage of little dependence on its ambient environment condition.[2] Most water wave energy is distributed in the offshore area benefiting the wave energy conversion as well as equipment maintenance,[3] and the wave transport from open sea to the shore is characterized by a relatively simple direction. Such clean, abundant, and random distributed energy has been exploited by the electromagnetic generator (EMG) technology.[4] However, the EMG is often criticized by its disadvantages of high cost, easily corroded, and low efficiency at the frequency of ocean wave.[5]

Recently, triboelectric nanogenerator (TENG), adopting the mechanism of Maxwell's displacement current, has been approved as an effective technology to harvest the water wave energy.[5,6] The TENG can produce higher output performance than the EMG at low frequency, demonstrating its killer application in harvesting low-frequency water wave energy. Various approaches, such as structural design, systematic optimization, material treatment, atmosphere modulation, external excitation, and so on, have been employed to enhance the output performance of TENG in harvesting the water wave energy.[7] However, owing to limitations from the low surface charge density, low oscillation frequency, poor surface contact, dielectric shielding of water, insufficient space utilization, and lacking stability, etc., the average performance of the TENG in real water waves is still not high. Possible solutions involves integrating multiple TENG units into an enclosed space as much as possible for raising the space utilization,[8] introducing a spring to improve the oscillation frequency,[9] optimizing the structure for responding to multiform excitations,[10] and designing an air gap structure between the TENG main body and water. The air gap structure has been proved to be capable of decreasing the dielectric shielding effect from the water in the previous work.[11]

In this work, a spherical whirling-folded TENG with a 3D-printed substrate was designed and fabricated to harvest the water wave energy. The output performance of the

J. An, Z. M. Wang, Prof. T. Jiang, X. Liang, Prof. Z. L. Wang
CAS Center for Excellence in Nanoscience
Beijing Key Laboratory of Micro-Nano Energy and Sensor
Beijing Institute of Nanoenergy and Nanosystems
Chinese Academy of Sciences
Beijing 100083, China
E-mail: zlwang@gatech.edu
J. An, Z. M. Wang, Prof. T. Jiang, X. Liang, Prof. Z. L. Wang
School of Nanoscience and Technology
University of Chinese Academy of Sciences
Beijing 100049, China
Prof. Z. L. Wang
School of Materials Science and Engineering
Georgia Institute of Technology
Atlanta, GA 30332-0245, USA
The ORCID identification number(s) for the author(s) of this article can be found under https://doi.org/10.1002/adfm.201904867.

DOI: 10.1002/adfm.201904867

WF-TENG was quantitatively characterized in the standard water wave tank with adjustable and controlled wave frequency and height. Besides, the influences of the water wave status on the output properties of a single face TENG and an overall device were systematically investigated, as well as the internal structural parameters. A theoretical dynamical analysis on the TENG motion state was carried out to understand the impacting principle of water waves. More importantly, a self-charge-supplement network including a charge-supplement TENG (CS-TENG) and surrounding main TENGs (M-TENGs) was proposed to maintain the high performance and stability of TENG network simultaneously, and the working principle was preliminarily revealed. Finally, the applications of the WF-TENG device in self-powered temperature sensing and self-powered monitoring on working state of device or network were demonstrated.

2. Results and Discussion

A spherical whirling-folded TENG consisting of a supporting spherical shell and internal main part of power generation was designed for harvesting the water wave energy, as schematically shown in **Figure 1**a. The diameter of outside acrylic spherical shell is 10 cm, and a square acrylic frame is used to support the internal TENG. An air gap between the internal TENG and the bottom of spherical shell is designed to minimize the dielectric shielding effect from the water. The whirling-folded TENG structure with two basic units in each face can be clearly viewed from the enlarged figure. Both sides of a 3 mm thick vortex skeleton fabricated by 3D printing technology are adhered by two printed circuit board (PCB) strips. The 3D-printed vortex skeleton as the TENG substrate is made of polylactic acid (PLA), which is a kind of environmentally friendly material with excellent mechanical properties. The photographs of PLA substrate, PCB strip, and the pattern of PCB strip with Cu electrodes deposited on the Kapton substrate are shown in Figure S1 of the Supporting Information. One PCB strip is attached by a 30 μm thick fluorinated ethylene propylene (FEP) film as the triboelectric layer. In this work, we fabricated the spherical WF-TENG device with five basic units in each face, as shown from the photograph in Figure 1b. Thus, there are 20 basic TENG units in total, and the five units in each face are connected in parallel. A mass block placed in the center of PLA skeleton can rock when imposed external triggering, driving the tribosurfaces to contact and separate. And a rubber band is introduced to construct a suspended oscillator structure for improving the vibration of mass block. Further details of fabrication process can be found in the Experimental Section.

Figure 1c shows the working principle of WF-TENG in a contact–separation working mode based on the contact electrification between the innerlayer Cu and FEP film. When

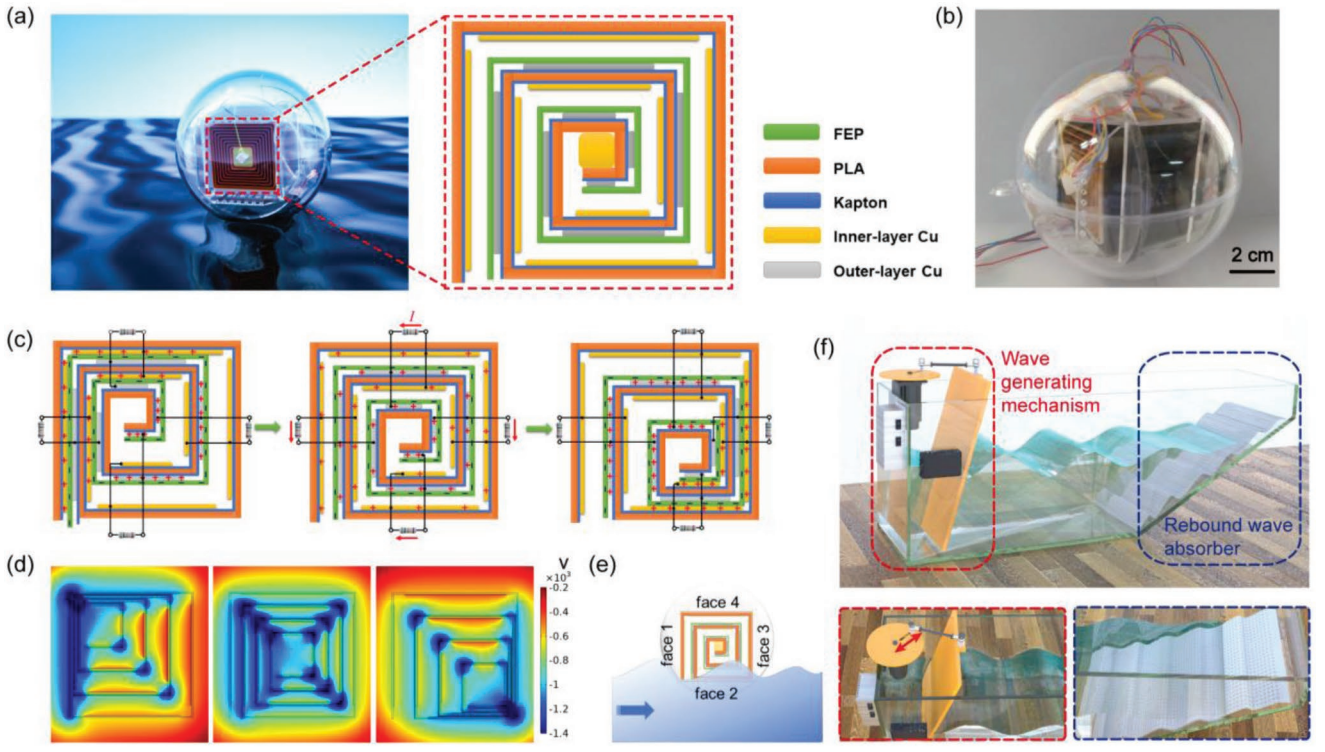

Figure 1. a) Schematic diagram of a spherical whirling-folded TENG floating on the water surface, and schematic representation for the internal TENG structure with two basic units in each face. b) Photograph of the WF-TENG device as fabricated. c) Schematic working process of the device for different mass block positions. d) Corresponding electric potential distributions for the WF-TENG at different mass block positions calculated by COMSOL simulations. e) Schematic illustration for the order of four faces in the TENG. f) Schematic structure of the water tank for generating water waves. The lower part shows the enlarged views of wave generating mechanism and rebound wave absorber.

the enclosed mass block rocks to the left-top position (state i) under an external triggering such as the water wave impact, the innerlayer Cu and FEP contact in both the left and top faces, generating positive charges on the Cu and negative charges on the FEP surface. For convenience, the four faces of TENG are marked as shown in Figure 1e. At the same time, the opposite faces (face 2 and face 3) receive the maximum separation, and positive charges are induced on the outerlayer Cu. When the mass block rocks to the middle position (state ii), the change of potential difference between two electrodes drives the eletron flowing through the external circuit, generating the current. The current direction in face 1 and face 4 is from the innerlayer Cu to the outerlayer Cu, which is opposite to that in face 2 and face 3. The current does not stop flowing until the mass block arrives at the right-bottom position (state iii), where the triboelectric layers in the face 1 and face 4 are maximumly separated, while those in the face 2 and face 3 contact closely. As it further moves to the moderate separating state, the current flows back with a reversed direction. In the periodic motion process of mass block, an alternating current is generated. The corresponding electric potential distributions for the WF-TENG at different mass block positions were also simulated by the finite element method to reveal the electricity generation principle (Figure 1d). In addition, two PCB strips on both sides of the skeleton will decrease its elastic force, so we introduce the rubber band to provide the auxiliary elasticity. Assisted by the elasticity of 3D-printed skeleton and rubber band, the mass block can oscillate multiple times at one stimulation of water waves to improve the average electric output.

The real water waves, under a natural circumstance, vary randomly all the time, prohibiting accurate artificial simulations on them. However, a series of standard water waves with different wave heights and frequencies can be detached from any kind of random waves. Standard wave tank experiment will facilitate the quantitative characterization of WF-TENG performance. Thus a water wave tank with two main parts (wave generating mechanism and rebound wave absorber as shown in Figure 1f) was built to generate standard water waves. The wave generating mechanism could generate water waves with adjustable and controlled wave parameters, such as the wave frequency and wave height. The rotation of acrylic disk in the crank linkage mechanism driven by a rotary motor induces the swinging of push plate back and forth. One wave will be generated in each rotation cycle. The rebound wave absorber, as its name implies, is used to prevent the waves from bouncing at the end of tank to disturb the advancing waves. The photographs and the structural layout of the water wave generating system and the water tank equipped with a wave-absorbing device at its end are also provided in Figure S1d–f of the Supporting Information.

Figure 2a shows the schematic illustrations of generating water waves with different wave frequencies (f) and wave heights (H). The wave frequency and height can be controlled independently by the following wave control method. Through adjusting the time interval between two rotation cycles, the distance between two adjacent wave crests can be changed, and waves with different frequencies are obtained without affecting the wave height. The wave frequency can be calculated based on the rotation speed of the disk and the dwell time. On the other hand, the wave height depends on the swing amplitude of the push plate, which is controlled by the crank length. The larger the amplitude, the higher the generated waves. Therefore, different wave heights can be realized by adjusting the crank length. The wave height was evaluated from videos of water wave motions.

The output performance of the spherical WF-TENG device under the water waves with different wave heights and frequencies was characterized. Before the measurements, the device was well sealed and waterproofed by polymer glues to prevent the effect of moisture. The five basic units in each face of the spherical TENG are electrically connected in parallel directly, due to their synchronous motion assisted by the elasticity of the 3D-printed skeleton. The performances of the four faces were separately investigated first of all because of their different positions. Generally, actual ocean waves are in a low-frequency state below 2 Hz, but have a broad height range from 0 to 1 m. In this work, the wave frequency range of 0.5–1.5 Hz and wave height range of 6–10 cm were chosen as representatives to reveal their influences on the device performance. To mimic practical networking state, two counterweight spheres were connected on both sides of our device for measurements (Figure S1e, Supporting Information).

The output currents for faces 1–4 of the WF-TENG were measured at various wave heights, as shown in Figure 2c. The wave frequency was chosen as 1.1 Hz, and the mass of the copper block enclosed inside the spherical shell with a diameter of 10 cm was fixed at 123.6 g. Apparently, we can conclude that the output current increases with increasing the wave height from 6 to 10 cm for all the four faces. That is because the increased impact force of water waves at a larger wave height intensifies the rocking movement of mass block. The face 4 exhibits the lowest output current, in which the contact–separation of triboelectric layers at the top position is hindered by the gravity. The output voltage and transferred charge for the four faces were also found to have the similar tendency with the increase of the wave height, as presented in Figure S2a,b of the Supporting Information.

On the other hand, the dependence of the output performance on the water wave frequency was investigated at a fixed wave height of 10 cm. As shown in Figure 2d, while raising the wave frequency from 0.8 to 1.5 Hz, the output current first increases, and then decreases for all the four faces. There exists an optimum frequency to get the maximum current. The optimum frequency of faces 1, 2, 4 is 1.2 Hz, while that of the face 3 is 1.4 Hz, which is related to the natural frequency of each face in the WF-TENG device. The maximum current is over 100 μA obtained at the faces 1 and 3. Besides the output current, the influences of the wave frequency on the output voltage and transferred charge are not significant (Figure S2c,d, Supporting Information), except for the face 4, where an optimum frequency of 1.2 Hz exists. Subsequently, to get the motion path of inner mass block, we collected the output voltage and transferred charge synchronously for four faces of WF-TENG. The output voltage exhibits regularity of periodicity with the colored area making up a cycle as shown in Figure 2e. The motion characteristic of the mass block can be analyzed from the profiles of transferred charge

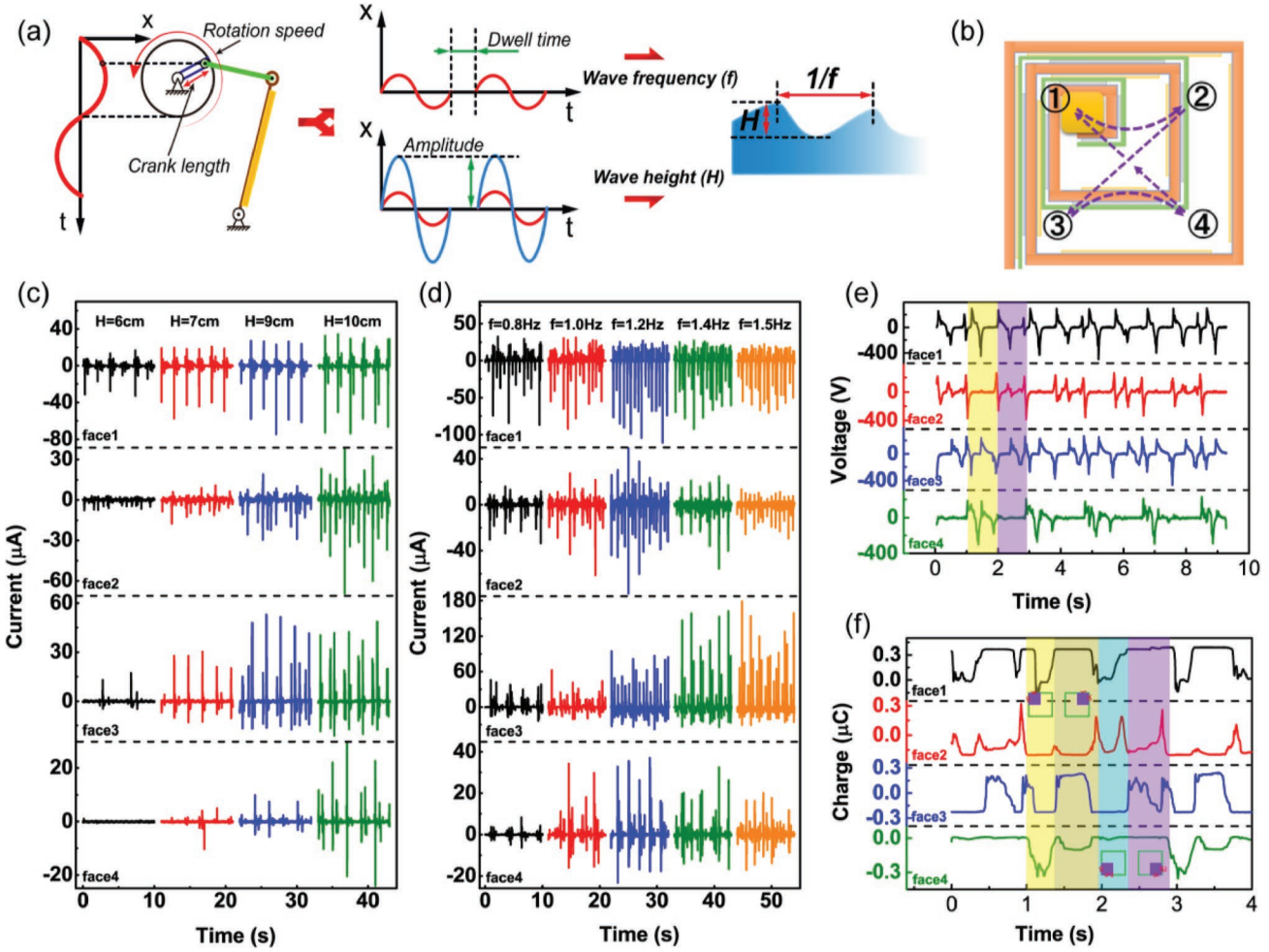

Figure 2. a) Schematic illustration of wave control method for generating water waves with different wave frequencies (*f*) and wave heights (*H*). b) Motion path of internal mass block in one cycle judged from the output signals. c,d) Output current of the TENG units in the four faces of the device at different wave conditions: (c) variable wave height with a fixed frequency of 1.1 Hz; and (d) variable wave frequency with a fixed wave height of 10 cm. e) Output voltage and f) transferred charges acquired synchronously for four faces of WF-TENG. f) The colored areas display the output signals in one motion cycle, and different colors represent different mass block positions (see inset).

according to the rule that the transferred charge arrives at the peak value when the face is compressed by mass block. In Figure 2f, different colors represent different positions of mass block as shown in the inset. Finally, we summarized and got a funnel-shape motion path for the inner mass block (Figure 2b).

In the practical application of the WF-TENG, the four faces were respectively connected to a full-bridge rectifier due to their asynchronous motions. After that, they were connected in parallel to improve the performance. The output performance of the whole WF-TENG with four faces connected in parallel for various water wave heights and frequencies were investigated, as shown in **Figure 3**. Figure 3a and Figure S3a (Supporting Information) show the rectified output current and output voltage as functions of the wave height at a fixed wave frequency of 1.1 Hz. It is apparent that the output current and voltage both increase with the increment of the wave height, similar to the case of a single face. However, owing to the superposition of the outputs from four faces, the density of pulse peaks is obviously higher than that of a single face, implying that the average power will be increased by connecting four faces in parallel. Then the impact of the water wave frequency on the output current and voltage resembles to the case of a single face as well. From Figure 3b and Figure S3b (Supporting Information), the optimum wave frequency of 1.4 Hz exists for the whole device to achieve the maximum current (about 85 μA) and voltage (about 450 V).

The resistance dependence of the output performance for the whole WF-TENG with four faces connected in parallel was also measured. The average power was calculated by the output energy per unit time, where the energy was obtained through the time integration of square of output current at a load resistance multiplied by the resistance during 45 s. Figure 3c,d exhibits the obtained average power–resistance profiles of the whole WF-TENG device at various wave heights and wave frequencies. The maximum average power increases with the wave height, approximately demonstrating a linear relation

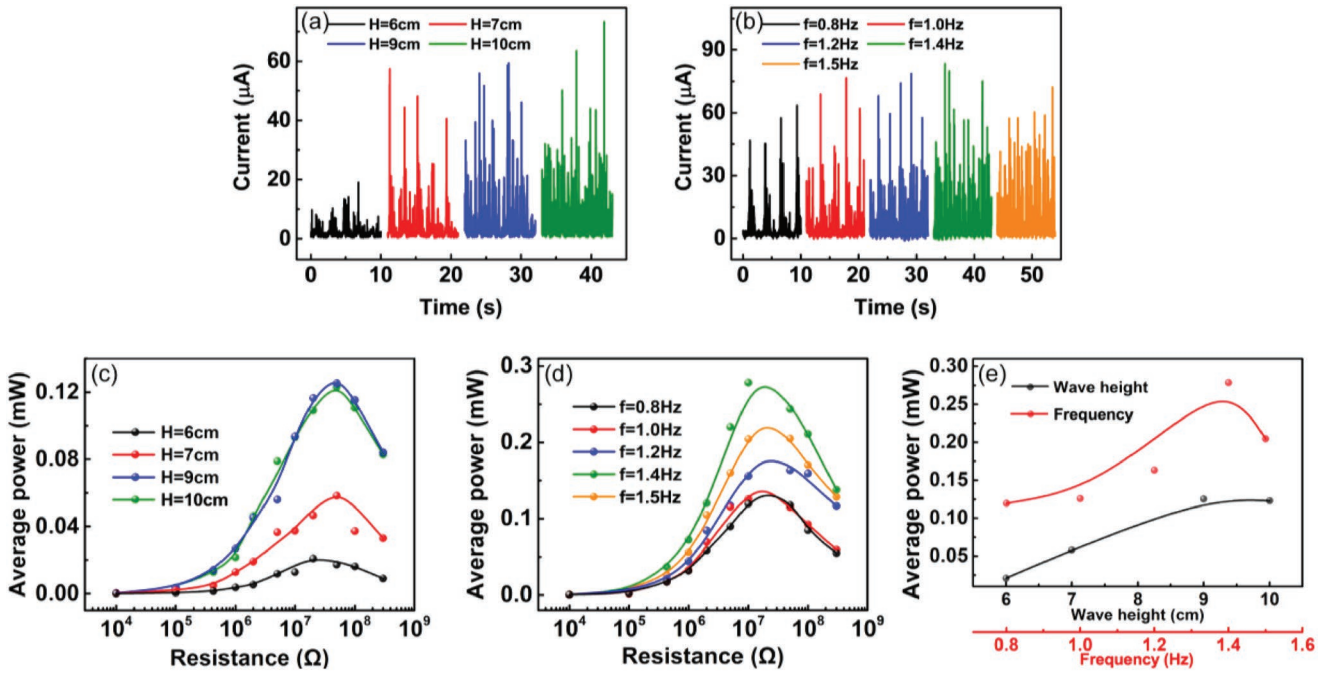

Figure 3. a) Rectified output current of the WF-TENG device with four faces connected in parallel for various water wave heights at the fixed wave frequency of 1.1 Hz. b) Rectified output current of the whole device for various wave frequencies at the fixed wave height of 10 cm. c,d) Average power–resistance profiles of WF-TENG with four faces connected in parallel: (c) at different wave heights (f = 1.1 Hz), (d) at different wave frequencies (H = 10 cm). The copper block mass and spherical shell diameter are 123.6 g and 10 cm, respectively. e) Summarized dependence of average power on the water wave height and frequency.

from H = 6 cm to H = 9 cm and getting saturated after 9 cm (Figure 3e), which is ascribed to that the amplitude of device reaches its limitation when the wave height exceeds 9 cm. For the influence of the wave frequency, the average power arrives at the highest value of 0.28 mW at the optimal wave frequency of 1.4 Hz (Figure 3d,e). The peak power for the device is about 6.5 mW at the matched resistance of 10 MΩ at 1.4 Hz, which was obtained by the peak current square multiplied by the resistance for comparison (Figure S4, Supporting Information). The corresponding average power density and peak power density were calculated to be 0.54 and 12.4 W m^{-3} according to the sphere volume. Due to the excellent performance, one WF-TENG can easily light up more than 460 light emitting diodes as shown in Video S1 of the Supporting Information.

Aside from the external water wave conditions, the internal structure parameters such as the diameter of spherical shell, mass of copper block, and the pitch of vortex structure in the WF-TENG are other critical factors governing the output performance of device. Under the optimized water wave conditions (H = 10 cm, f = 1.4 Hz), the output current, output voltage, and average power of the whole device with four faces connected in parallel were experimentally studied for different copper block masses and spherical shell diameters, as shown in Figure S5 of the Supporting Information. The copper block mass of 45.5, 67.8, 102.4, 123.6 g, and the spherical shell diameter of 10, 14, and 17 cm were chosen for instance. It was found that increasing the copper block mass and decreasing the spherical shell diameter are beneficial to increase the average output performance. Besides, the effect of the pitch of vortex structure on the open-circuit voltage was revealed via the COMSOL Multiphysics (Figure S6, Supporting Information). The increase in the pitch can lead to the increment in the maximum voltage, which becomes less obvious at a larger pitch over 3 mm. Nevertheless, the increased pitch also causes the elasticity of the 3D-printed skeleton decreased and the space utilization ratio diminished. Therefore, in this work, the small pitch of 2 mm for the whirling structure was chosen. More layers will lead to a longer motion distance of inner mass block and a decrease of stiffness of 3D-printed skeleton, which is adverse for output performance. However, these two inclinations are not obvious when the layer number is small. And, the performance will be greatly improved due to the significant increasement of surface areas.

In the experiments, for the stability and durability of the device, actually, the generation of water waves needs striking impact between water and the push plate, which will cause visible damage to the fragile acrylic water tank, so we did not execute the durability experiments. Besides, our TENGs are based on the contact–separation working mode possessing the merit of low friction loss of two contact parts, which has been verified by previous works. The durability of our device mainly depends on the stiffness of acrylic frame and spherical shell as well as the ability of 3D-printed skeleton to resist bending fatigue. Thus the utilization of strong materials such as metal for the structure will elongate the lifetime of this device.

To further understand the impacting principles of the wave height and wave frequency on the TENG outputs, a dynamical analysis for the motion of the TENG device under the water wave actions was proceeded. Our spherical WF-TENG was connected to two counterweight spheres on both sides to reflect the

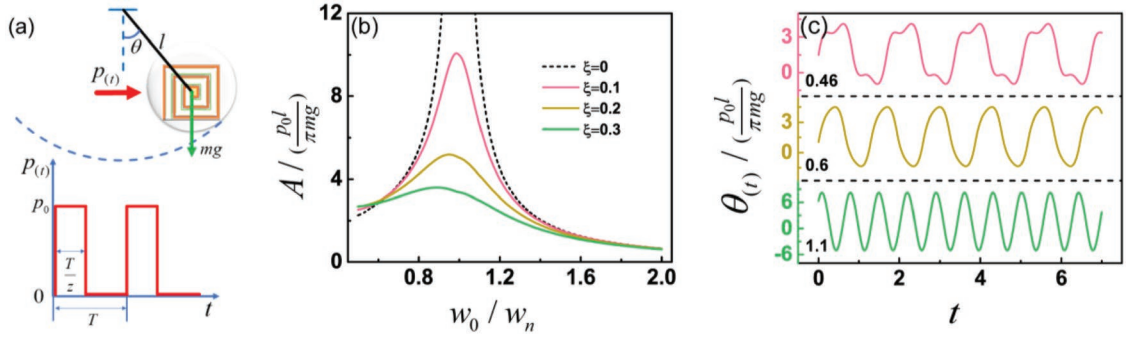

Figure 4. a) Schematic diagram of dynamical analysis of the WF-TENG subjected to a periodic excitation of unidirectional square waves. b) Amplitude of the device at the steady state with respect to the frequency ratio of ω_0/ω_n, calculated for various damping ratios ξ. The rope length l is fixed as 0.15 m, and the nature frequency ω_n is fixed as 8.1 rad s^{-1}. c) Calculated steady-state vibration waveform of the device for different ω_0/ω_n values (0.46, 0.6, and 1.1) at a fixed damping ratio of 0.1.

networking state. The periodic motion of the TENG in the networking state under a periodic wave impact can be reasonably simplified as a forced vibration of a pendulum, which is subjected to an impact of periodic unidirectional square waves, as schematically shown in **Figure 4**a. The periodic excitation function $p_{(t)}$ has an amplitude of p_0, and a duty ratio of $1/z$, θ is the swing angle of the TENG, mg is the gravity of TENG, l is the rope length, and T is the impact period. The equation of $p_{(t)}$ can be expressed as the following form by Fourier series expansion[12]

$$p_{(t)} = \frac{a_0}{2} + \sum_{n=1}^{\infty}\left(a_n \cos nw_0 t + b_n \sin nw_0 t\right)$$
$$\begin{cases} a_0 = \dfrac{2p_0}{z} \\ a_n = \dfrac{2p_0}{Tnw_0}\sin\left(\dfrac{2\pi n}{z}\right) \\ b_n = \dfrac{2p_0}{Tnw_0}\left[1-\cos\left(\dfrac{2\pi n}{z}\right)\right] \end{cases} \quad (1)$$

where ω_0 is the angle frequency of the excitation. The motion differential equation of this single-degree-of-freedom linear system can be given by[12]

$$m\ddot{\theta} + c\dot{\theta} + k\theta = p_{(t)} \quad (2)$$

where c is the damping parameter, and k is the elastic coefficient of the pendulum. Combining Equations (1) and (2), we can solve the differential equation and get the equation of $\theta_{(t)}$ for a duty ratio of 0.5

$$\theta_{(t)} = \frac{p_0}{\pi w_n^2 m}\left[\frac{\pi}{2} + \sum_{n=1,3,5}^{\infty}\frac{2\sin(nw_0 t - \psi_n)}{n\sqrt{\left(1-\overline{w}_n^2\right)^2 + \left(2\xi\overline{w}_n\right)^2}}\right] \quad (3)$$

where $w_n = \sqrt{\dfrac{g}{l}}$ is the natural frequency of device, $\overline{w}_n = \dfrac{nw_0}{w_n}$, $\psi_n = \arctan\dfrac{2\xi\overline{w}_n}{1-\overline{w}_n^2}$, and ξ is the damping ratio. The detailed derivation process is available in Notes for Figure S7 of the Supporting Information.

In previous experiments, the equivalent length of rope is about 0.15 m, so the natural frequency ω_n of the device can be estimated to be 8.1 rad s^{-1} (about 1.3 Hz). By substituting the values of the two parameters in Equation (3), we calculated the device amplitude at the steady state with respect to the frequency ratio of ω_0/ω_n for various damping ratios ξ, as shown in Figure 4b. A constant of $\dfrac{p_0 l}{\pi mg}$ is extracted for the amplitude, where the excitation amplitude p_0 and device mass m are undetermined. The device amplitude is inversely proportional to m, but directly proportional to p_0 associated with the generated wave height. Therefore, the higher device amplitude at a larger wave height is the reason for generating higher electric outputs (Figure 3a,c). It can be found that as the basic frequency of excitation is approaching the natural frequency (ω_0/ω_n = 1.0), the amplitude of system reaches the maximum, referred as the resonance point. In other words, an optimum excitation frequency exists for the device to get the maximum amplitude, therefore, leading to the highest outputs. We can also view the effect of the damping ratio on the motion amplitude. When there is no damping, the amplitude at the resonance point can reach the infinity, and while increasing the damping ratio, the maximum amplitude decreases gradually. In addition, the steady-state vibration waveform of the device varies with the change of the ω_0/ω_n ratio (Figure 4c). At a lower ω_0/ω_n of 0.46, there are two small peaks on top of every main peak in the $\theta_{(t)}$ profile, and they will merge into one peak with increasing ω_0/ω_n. The small peaks appearing at lower ω_0/ω_n may be induced by the system natural flexibility, which improves the vibration frequency of system at a low-frequency excitation.

For practical applications of the TENG device, maximizing the output performance is highly desirable. Besides the external water wave controlment or internal structural optimization, external charge supplement is another effective strategy to enhance the TENGs outputs. Recently, a charge excitation TENG system with external charge excitation has been reported, and an ultrahigh charge density of 1.25 mC m^{-2} was realized in ambient condition.[13] Here, as schematically shown in **Figure 5**a, we propose a self-charge-supplement TENG network for scavenging large-scale blue energy, which consists of a

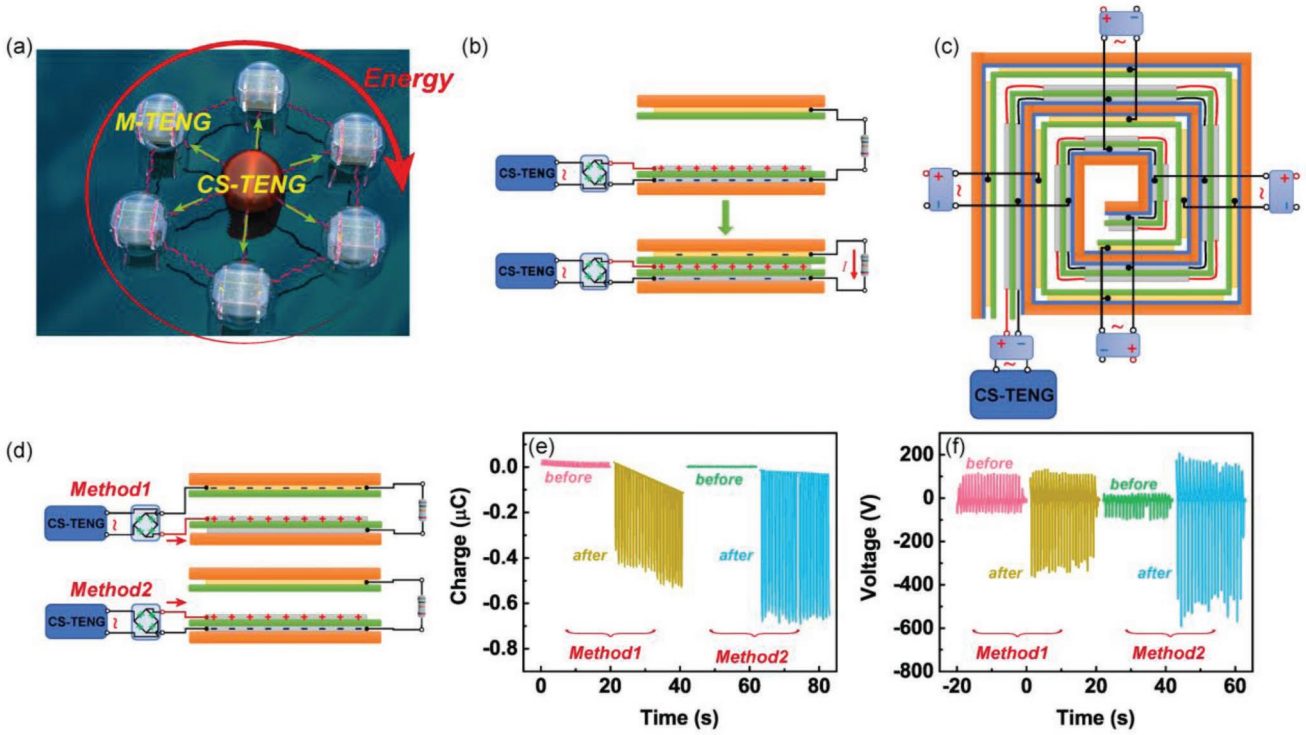

Figure 5. a) Schematic diagram of a self-charge-supplement TENG network consisting of a CS-TENG and several M-TENGs, proposed for harvesting large-scale blue energy. b) Working process of the M-TENG with a floating structure supplemented by the CS-TENG. c) Schematic diagrams of the fabricated charge-replenishable WF-TENG and the circuit connection. d) Schematic illustration for two kinds of connection manners between the CS-TENG and M-TENG. e) Transferred charge and f) output voltage for one face of the charge-replenishable WF-TENG before and after the charge supplement by two methods at the separation state of TENG.

CS-TENG and several M-TENGs. During the function process of the TENG network, the CS-TENG can supplement charges for the M-TENGs continuously to prevent performance deterioration resulting from the charge dissipation. Maintaining the high performance of TENG network through the self-charge-supplement approach demonstrates the obvious merits such as high stability, reliability, and maintain-free. Generally, the CS-TENG produces a high voltage by connecting multiple TENG units in series or using a voltage-multiplying circuit, which is easily accessible and beneficial for the charge injection into the M-TENG. The output performance of M-TENG is restricted by the voltage of CS-TENG as well as the nature of insulating material in the M-TENG, because high voltage may cause material breakdown and damage the TENG. Therefore, the selection of robust voltage-withstand materials for M-TENG is critical to improve the TENG network performance.

The M-TENG attributes to a floating electrode structure to store and bind charges for electrostatic induction, similar to the structure in the previous work.[13] Each basic unit consists of three electrode layers and two dielectric layers, as shown in Figure 5b. The lower two electrodes separated by one insulating dielectric layer are connected to the CS-TENG via the rectifier, while the bottom and top electrodes are connected to external load to output the electric energy. The surface of the top electrode is attached by another insulating layer (Kapton is selected in this work). With the rectifier, positive and negative charges are pumped into the middle and bottom electrode layers, respectively. When the upper part of M-TENG unit moves downward and gets close to the lower part, the change in potential difference between the bottom and top electrodes drives the current flow from the top to the bottom layer through the external load. The periodic contact–separation generates periodic alternating current.

In the experiments, the CS-TENG employs the contact–separation-mode WF-TENG fabricated above, while the M-TENG has a relatively complicated structure as shown in Figure 5c. The M-TENG is also a whirling-folded TENG built with the basic units as illustrated in Figure 5b. In the charge-replenishable WF-TENG, all of the floating Cu and outerlayer Cu electrodes are respectively connected in series, and then connected to the CS-TENG. And the four faces are also rectified before the parallel connection. The M-TENGs can distribute around the CS-TENG to capture the water wave energy and maintain its high charge density by receiving the charges from CS-TENG.

We also explored the influence of the connecting manner between the CS-TENG and M-TENG. As shown in Figure 5d, in Method 2, the lower two electrodes of M-TENG are connected to the CS-TENG, while the top and middle electrodes are connected as Method 1. At the contact state of M-TENG, the two methods are almost the same due to the symmetrical structure. However, it is necessary to realize the charge supplement at the separation state of M-TENG, because the charge supplement occurs in the working process of TENG network, and the motions of the CS-TENG and M-TENGs are asynchronous. When there exists a maximum separation for the M-TENG

(restricted by the outer spherical shell and square frame) in Method 1, the capacitance formed by the top and middle electrodes reaches its minimum value, unfavorable to the charge injection. By contrast, the charge injection can be normally carried on in Method 2, since the capacitance formed by the lower two electrodes almost keeps unchanged. To further compare the two charging methods, the transferred charge and output voltage for one face in the M-TENG before and after the charge supplement by the two methods were measured as shown in Figure 5e,f and Figure S8 (Supporting Information). At the maximum separation state, higher transferred charge and output voltage can be obtained for Method 2. Detailed finite element simulations and theoretical analysis for comparing the two methods were also carried out, as shown in Figures S9–S11 of the Supporting Information.

Finally, the applications of the WF-TENG in powering portable electronics by harvesting ambient water wave energy to realize self-powered sensing and monitoring were demonstrated. A digital thermometer with a temperature sensor was utilized to detect the water temperature, and an accelerometer combined by a single-chip microcomputer unit (MCU) was applied to monitor the working state of TENG device or network. Considering electronics cannot be directly powered by the TENG due to the low excitation frequency of wave, the capacitor is required to serve as an energy storage and buffer unit. **Figure 6**a plots the charging performance of as-fabricated WF-TENG device with parallel connection of four faces for various capacitors driven by the water waves. The water wave adopts the optimal condition mentioned above. As the capacitance increases, the charging voltage decreases with a reduced charging speed. The voltage of the capacitor of 10 μF can be raised to 22.7 V within 60 s, corresponding to an output charge of 227 μC. Then the WF-TENG device was used to power a digital thermometer through connecting a capacitor of 220 μF. The charging and discharging processes of the capacitor to power the thermometer are presented in Figure 6b. After the capacitor is charged to 1.0 V, the thermometer, connected to the circuit, starts to measure the water temperature. Interestingly, the thermometer can continuously work and display the temperature value with the water wave motions, and the voltage on the capacitor is gradually saturated with a slight rise, implying that harvested energy exceeds the consumption. The photograph and video of the digital thermometer successfully powered by the water-wave-driven WF-TENG are shown in the inset of Figure 6b and Video S2 (Supporting Information).

Self-powered monitoring on the working state of TENG device or network plays an essential role for taking precautions to avoid damages caused by dramatic motions of water waves. Therefore, an accelerometer was embedded into the WF-TENG device to attain the motion information, as depicted in the photograph of Figure 6c. A capacitor of 440 μF was also packed inside the spherical shell to store the electric energy for

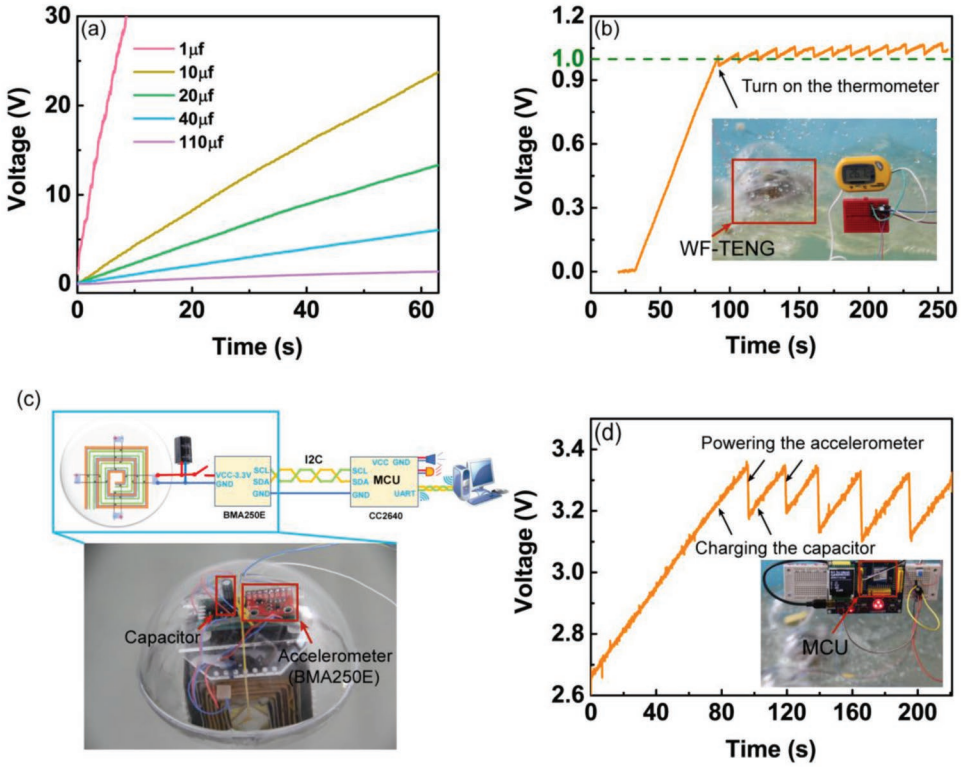

Figure 6. a) Charging voltage of various capacitors for as-fabricated WF-TENG device with parallel connection of four faces driven by the water waves. b) Charging and discharging process of the capacitor of 220 μF to power the thermometer. The inset is the photograph of the thermometer powered by one WF-TENG. c) Schematic diagram of the self-powered monitoring system on the working state of TENG device constructed by harvesting the water wave energy and the photograph for the WF-TENG device embedded by an accelerometer and a capacitor of 440 μF. d) Charging voltage profile of the 440 μF capacitor for several consequent working cycles of accelerometer. The inset shows the photograph of MCU sending sound and light alarm signals when the dip angle is too large, where the accelerometer is powered by the WF-TENG and sends the dip information to the MCU for processing.

powering the accelerometer (BMA250E). The accelerometer can transmit signals to the MCU (CC2640) for processing through the I2C bus. Once a dramatic motion of the TENG device (too large dip angle) is detected by the accelerometer, the MCU will send sound and light alarms or send signals to the remote monitoring room through the wireless transmitter. The self-powered monitoring system on the working state of TENG device constructed by harvesting the water wave energy is schematically shown in the upper part of Figure 6c. In order to construct a unified communication benchmark between the accelerometer and MCU, their GND ports need to be connected together, so that the MCU can obtain the dip angle information of WF-TENG device without providing an electric power to the accelerometer. Figure 6d exhibits the voltage on the capacitor during several consequent working cycles of accelerometer. After the 440 μF capacitor is charged to 3.3 V, by closing the switch, the accelerometer can be successfully powered to work for about 3 s to send the current dip information to the MCU. As long as the MCU detects irregular dip information, the sound and light alarms will be transmitted immediately as shown in the inset of Figure 6d and Video S3 (Supporting Information).

3. Conclusion

In summary, we demonstrated a spherical whirling-folded TENG consisting of a multilayered TENG structure with an elastic 3D-printed PLA substrate for harvesting the water wave energy. The output performance of a single WF-TENG was quantitatively characterized in a standard water-wave-generating tank. The effects of external water wave conditions and internal structural parameters on the electric outputs of device were investigated. Under the optimal wave conditions of 1.4 Hz (wave frequency) and 10 cm (wave height), a single spherical WF-TENG device can deliver an average power of 0.28 mW and a peak power of 6.5 mW, corresponding to the power density of 0.54 and 12.4 W m^{-3}. A dynamical analysis for the motion of the TENG device under the water wave actions was theoretically carried out to reveal the impacting principles of the wave parameters. Besides, a self-charge-supplement TENG network with high output performance and stability was proposed toward scavenging large-scale blue energy. Finally, a digital thermometer and an MCU-integrated accelerometer were successfully powered by merely one single WF-TENG, suggesting extensive applications in self-powered hydrological sensing fields.

4. Experimental Section

Fabrication of the WF-TENG: First, a 3 mm thick 3D-printed vortex skeleton (5 cm × 5 cm × 5 cm) with a pitch of 2 mm served as the substrate of the internal TENG with five basic units in each face. One PCB strip (631 mm × 50 mm × 0.15 mm) with electrode patterns (12 μm thick) was adhered on the innerlayer of PLA skeleton. A 30 μm thick FEP film (631 mm × 50 mm) attached on the other PCB strip (572 mm × 50 mm) was adhered on the outer layer of PLA skeleton. Electrons were injected to the FEP surfaces to increase the surface charge density at a polarization voltage of 5 kV. Four sides of cubic skeleton were attached by sponge (5 cm × 5 cm) to decrease the impact on square acrylic frame. Then, the internal TENG supported by acrylic frame was packed into the acrylic spherical shell, followed by the sealing and waterproofing process using polymer glues. All the TENG units in each face of the WF-TENG were connected in parallel by the circuit on PCB, and the four faces were respectively connected by a rectifier bridge before their parallel connection. For the charge-replenishable WF-TENG, the fabrication method is similar, but the PCB strip attached on the outer layer of skeleton has three layers (Cu–Kapton–Cu) without FEP film, and the other PCB strip on the innerlayer of skeleton is covered by a Kapton film.

Electric Measurements of the TENG Device: The electric outputs of the WF-TENG device were measured in the regular water waves by combining the wave generating mechanism and rebound wave absorber. The swing of push plate is realized through the rotation of crank, which is controlled by a programmable digital controller. The rebound wave absorber comprises a slope covered with porous cushion. The output current, transferred charge of the device, and charging voltage on a capacitor were all measured by a current preamplifier (Keithley 6514 System Electrometer), while the output voltage of the TENG device was measured by a digital oscilloscope (Agilent InfiniiVision 2000×).

Finite Element Simulations via *COMSOL*: 2D models of the WF-TENG with three basic units in each face for the pitches of 2, 3, 4, 5, and 6 mm were respectively built by the COMSOL software. The thickness of every layer matches the actual thickness in the device. A surface charge density of −4.2 μC m^{-2} was set for the FEP film, and the same amount of positive charges was set on the innerlayer Cu electrode due to the charge conservation. The electric potential distributions were calculated at different mass block positions along the diagonal direction, and the open-circuit voltage was obtained through the potential difference between two electrodes. As for the simulations of two charge-supplement methods, a contact–separation mode TENG model was built which has the same arrange order and thickness as the actual device for every layer. The injected charge density was set as 240 μC m^{-2}.

Supporting Information

Supporting Information is available from the Wiley Online Library or from the author.

Acknowledgements

J.A., Z.W., and T.J. contributed equally to this work. Supports from the National Key R&D Project from Minister of Science and Technology (2016YFA0202704), the National Natural Science Foundation of China (Grant Nos. 51432005, 51702018, and 51561145021), and the "thousands talents" program for the pioneer researcher and his innovation team are appreciated. The authors also thank Jinhui Nie and Jiajia Shao for device fabrications and measurements.

Conflict of Interest

The authors declare no conflict of interest.

Keywords

blue energy, self-charge-supplement TENG network, self-powered sensing/monitoring, water wave energy harvesting, whirling-folded triboelectric nanogenerator

Received: June 18, 2019
Revised: July 12, 2019
Published online:

[1] a) N. Duić, M. da Graça Carvalho, *Renewable Sustainable Energy Rev.* **2004**, *8*, 383; b) T. Senjyu, D. Hayashi, A. Yona, N. Urasaki, T. Funabashi, *Renewable Energy* **2007**, *32*, 1917.
[2] a) A. Von Jouanne, *Mech. Eng.* **2006**, *128*, 24; b) J. Tollefson, *Nature* **2014**, *508*, 302; c) Z. L. Wang, *Nature* **2017**, *524*, 295.
[3] S. Z. I. R. Young, A. V. Babanin, *Science* **2011**, *332*, 451.
[4] a) S. H. Salter, *Nature* **1974**, *249*, 720; b) R. Henderson, *Renewable Energy* **2006**, *31*, 271; c) A. F. d. O. Falcão, *Renewable Sustainable Energy Rev.* **2010**, *14*, 899.
[5] Z. L. Wang, *Mater. Today* **2017**, *20*, 74.
[6] a) Z. L. Wang, *Faraday Discuss.* **2014**, *176*, 447; b) Z. L. Wang, J. Chen, L. Lin, *Energy Environ. Sci.* **2015**, *8*, 2250; c) W. Tang, T. Jiang, F. R. Fan, A. F. Yu, C. Zhang, X. Cao, Z. L. Wang, *Adv. Funct. Mater.* **2015**, *25*, 3718; d) H. Zou, Y. Zhang, L. Guo, P. Wang, X. He, G. Dai, H. Zheng, C. Chen, A. C. Wang, C. Xu, Z. L. Wang, *Nat. Commun.* **2019**, *10*, 1427; e) Z. L. Wang, T. Jiang, L. Xu, *Nano Energy* **2017**, *39*, 9; f) F.-R. Fan, Z.-Q. Tian, Z. L. Wang, *Nano Energy* **2012**, *1*, 328; g) J. Nie, Z. Wang, Z. Ren, S. Li, X. Chen, Z. L. Wang, *Nat. Commun.* **2019**, *10*, 2264; h) Z. Ren, J. Nie, L. Xu, T. Jiang, B. Chen, X. Chen, Z. L. Wang, *Adv. Funct. Mater.* **2018**, *28*, 1805277; i) C. K. Jeong, K. M. Baek, S. Niu, T. W. Nam, Y. H. Hur, D. Y. Park, G. T. Hwang, M. Byun, Z. L. Wang, Y. S. Jung, K. J. Lee, *Nano Lett.* **2014**, *14*, 7031; j) H. S. Wang, C. K. Jeong, M.-H. Seo, D. J. Joe, J. H. Han, J.-B. Yoon, K. J. Lee, *Nano Energy* **2017**, *35*, 415.
[7] a) Z. Wu, H. Guo, W. Ding, Y. C. Wang, L. Zhang, Z. L. Wang, *ACS Nano* **2019**, *13*, 2349; b) J. Wang, L. Pan, H. Guo, B. Zhang, R. Zhang, Z. Wu, C. Wu, L. Yang, R. Liao, Z. L. Wang, *Adv. Energy Mater.* **2019**, *9*, 1802892; c) M. L. Seol, S. B. Jeon, J. W. Han, Y. K. Choi, *Nano Energy* **2017**, *31*, 233; d) B. D. Chen, W. Tang, C. He, C. R. Deng, L. J. Yang, L. P. Zhu, J. Chen, J. J. Shao, L. Liu, Z. L. Wang, *Mater. Today* **2018**, *21*, 88; e) T. Jiang, L. M. Zhang, X. Chen, C. B. Han, W. Tang, C. Zhang, L. Xu, Z. L. Wang, *ACS Nano* **2015**, *9*, 12562; f) L. Xu, T. Jiang, P. Lin, J. J. Shao, C. He, W. Zhong, X. Y. Chen, Z. L. Wang, *ACS Nano* **2018**, *12*, 1849; g) X. J. Zhao, J. J. Tian, S. Y. Kuang, H. Ouyang, L. Yan, Z. L. Wang, Z. Li, G. Zhu, *Adv. Mater. Interfaces* **2016**, *3*, 1600187.
[8] a) M. Xu, T. Zhao, C. Wang, S. L. Zhang, Z. Li, X. Pan, Z. L. Wang, *ACS Nano* **2019**, *13*, 1932; b) A. Ahmed, Z. Saadatnia, I. Hassan, Y. Zi, Y. Xi, X. He, J. Zu, Z. L. Wang, *Adv. Energy Mater.* **2017**, *7*, 1601705; c) X. Li, J. Tao, X. Wang, J. Zhu, C. Pan, Z. L. Wang, *Adv. Energy Mater.* **2018**, *8*, 1800705; d) X. Yang, L. Xu, P. Lin, W. Zhong, Y. Bai, J. Luo, J. Chen, Z. L. Wang, *Nano Energy* **2019**, *60*, 404.
[9] a) T. X. Xiao, X. Liang, T. Jiang, L. Xu, J. J. Shao, J. H. Nie, Y. Bai, W. Zhong, Z. L. Wang, *Adv. Funct. Mater.* **2018**, *28*, 1802634; b) X. Liang, T. Jiang, G. Liu, T. Xiao, L. Xu, W. Li, F. Xi, C. Zhang, Z. L. Wang, *Adv. Funct. Mater.* **2019**, *29*, 1807241; c) T. Jiang, Y. Y. Yao, L. Xu, L. M. Zhang, T. X. Xiao, Z. L. Wang, *Nano Energy* **2017**, *31*, 560.
[10] X. Wang, S. Niu, Y. Yin, F. Yi, Z. You, Z. L. Wang, *Adv. Energy Mater.* **2015**, *5*, 1501467.
[11] S. L. Zhang, M. Xu, C. Zhang, Y.-C. Wang, H. Zou, X. He, Z. Wang, Z. L. Wang, *Nano Energy* **2018**, *48*, 421.
[12] B. H. Tongue, *Principles of Vibration*, 2nd ed., Oxford University Press, Oxford **2002**, p. 518.
[13] a) W. Liu, Z. Wang, G. Wang, G. Liu, J. Chen, X. Pu, Y. Xi, X. Wang, H. Guo, C. Hu, Z. L. Wang, *Nat. Commun.* **2019**, *10*, 1426; b) L. Cheng, Q. Xu, Y. Zheng, X. Jia, Y. Qin, *Nat. Commun.* **2018**, *9*, 3773; c) L. Xu, T. Z. Bu, X. D. Yang, C. Zhang, Z. L. Wang, *Nano Energy* **2018**, *49*, 625.